RESEARCH ARTICLE

Journal of **RAMAN SPECTROSCOPY** WILEY

Development of non-destructive analytical strategies based on Raman spectroscopy and complementary techniques for Mars Sample Return tested on Northwest Africa 1950 Martian meteorite

Leire Coloma[1] | Cristina García-Florentino[1,2] | Jennifer Huidobro[1] |
Imanol Torre-Fdez[1] | Julene Aramendia[1,3] | Gorka Arana[1] | Kepa Castro[1] |
Juan Manuel Madariaga[1]

[1]Department of Analytical Chemistry,
Faculty of Science and Technology,
University of the Basque Country
UPV/EHU, Leioa, Spain

[2]Arcetri Astrobiology Laboratory, INAF -
Astrophysical Observatory of Arcetri,
Florence, Italy

[3]Aarhus Institute of Advanced Studies
(AIAS), Aarhus University, Aarhus,
Denmark

Correspondence
C. García-Florentino, Department of
Analytical Chemistry, Faculty of Science
and Technology, University of the Basque
Country UPV/EHU, Barrio Sarriena s/n,
48940 Leioa, Basque Country, Spain.
Email: cristina.garciaf@ehu.eus

Abstract

The Mars Sample Return (MSR) is a near future mission to return samples from the surface of Mars to the Earth. The field operations to carry out data collection, selection of the samples, and sampling procedure, mainly related to the CanMars MSR analog mission, are well-studied and published. In contrast, studies related to the methodology implemented to characterize the mineralogy of the returned samples are scarcer and focused on biosignature detection. This work presents a non-destructive analytical methodology based on Raman microscopy (single point and imaging), micro-energy dispersive X-ray fluorescence imaging analysis, and scanning electron microscopy coupled to energy dispersive spectroscopy that could be used as a first analytical characterization for the Martian samples that will be returned to the Earth in the upcoming MSR mission, before any destructive analysis. The analytical methodology has been tested on a fragment of the Northwest Africa 1950 Martian meteorite, which gives us a mineralogical characterization of the meteorite. This methodology also allowed to define several chemical reactions taking place in some of the mineral phases (olivines and ilmenite) of the meteorite. In addition to the geochemical characterization of the samples, the fact that this methodology allows to assess the chemical transformations in several minerals gives important clues for describing mineral processes and geological evolution that took place on Mars. This work also shows the advantages and disadvantages that each of the techniques employed has when performing a mineralogical characterization, the information that each one can provide and the importance of combining them.

1 | INTRODUCTION

The Mars Sample Return (MSR) is a near future proposed mission to return, for the first time, samples from the surface of Mars to the Earth, planned by the National Aeronautics and Space Administration (NASA) and the European Space Agency.[1] The samples are being selected and collected by the Perseverance rover (Mars 2020 mission). The first sample was collected on the first days of September 2021.[1] After the collection of the samples, the rover from the sample return mission will gather them and an ascent rocket will put them into Mars orbit. An orbiter, which is expected to be launched in 2026, will retrieve the sample container in Mars orbit, and the samples will be finally taken back to the Earth in 2031.[2]

These samples will be the first Martian samples on Earth that had not been previously subjected to the ejection impact and the entrance to Earth atmosphere as the Martian meteorites are. In this way, the minerals in the returned samples will not be overprinted by secondary processes such as impact metamorphism associated with ejection or terrestrial weathering. Observations of the non-impacted minerals and their textures will give us information about processes on Mars. In addition, these samples will belong to known locations on the surface of Mars, which will provide ground truth for remote sensing data. Once on Earth, the analysis campaigns will start with non-destructive analytical techniques due to the unique character of these samples and to the limited amount of each one, around 20 g.[3]

The field operations to carry out data collection, selection of the interesting samples, and sampling procedure are very well-studied and published, mainly related to the CanMars MSR analog mission.[4–9] However, the studies related to the methodology for the analyses of the samples once on Earth are scarcer and specially focused on biosignature detection. There is a study related to the biosignature detection by Mars rover equivalent instruments in samples from the CanMars mission[10] and a few works regarding the stability of life molecules (e.g., amino acids and nucleosides) on Mars analog minerals.[11,12] Nevertheless, few are the works dealing with the analytical methodology to thoroughly characterize those samples. Some of the possibilities have been suggested by the International Mars Architecture for the Return of Samples Working Group in their Phase 2 report.[13] Some of the non-destructive techniques proposed in that report are expensive as synchrotron sources

are required. In contrast, we have previously proposed a non-destructive analytical methodology based on the use of low-cost, micro-spectroscopic measurements such as high-resolution confocal Raman microscopy (single point and imaging analyses) and micro-energy dispersive X-ray fluorescence (μED-XRF) (imaging analysis).[14] The effectiveness of this analytical methodology was demonstrated using a previously characterized Martian meteorite, Dar al Gani 735 (DaG 735).[14] In that work, we were able to perform the same main mineralogical characterization of the meteorite that more traditional petrographic analyses and single-point measurements based techniques had previously performed. What is more, we were able to go deeper on its characterization describing the presence of several compounds not reported earlier for the DaG 735 or even for its paired fragments. In addition, we proposed it as a first quick and cost-effective characterization to distinguish between some of the original Martian compounds and new formed terrestrial compounds, based on imaging analyses. Imaging analyses provided information about the distribution of minerals, and high-resolution Raman allowed assessing Raman shifts in the signals of the minerals caused by the effect of temperature and pressure, provoking shock metamorphism on the minerals.[14]

Until Mars samples are on Earth, meteorites are the only samples originally from Mars to test the analytical methodology proposed in this work, in which the Northwest Africa 1950 (NWA 1950) meteorite was selected. In January and March of 2001, two stone pieces of 414 and 383 g, respectively, were found in the Atlas Mountain (Morocco, Northwest Africa),[15] although the exact location of the site of collection is unknown.[15] This meteorite is also called as "Jules Verne" in honor to his novel "The Chase of the Golden Meteor". This pseudonym is also registered in the official Meteoritical Bulletin N°88.[15] Gillet et al.[16] made a petrological characterization of the main mineral phases and determined the cosmic-ray exposure age, and the NWA 1950 was classified as a lherzolitic shergottite.[15,16] However, nowadays, it is recommended to use the term poikilitic shergottites that refers to their texture (as they contain some much larger grains that enclose many smaller grains of other minerals).[17] This change in nomenclature is because of the observation that the modal abundances of minerals in "lherzolitic" shergottites do not fall within the ranges defined for a lherzolite, according to the classification scheme of igneous rocks by Walton et al.[17] Although

basaltic and olivine-phyric shergottites show wide variation in mineralogy and petrology, a few number of poikilitic shergottites (the former lherzolitic shergottites) show very consistent characteristics.[18,19] The subtle mineralogical differences that have been defined are probably because of spatially variable cooling rates during the crystallization of the basaltic area or different degrees of re-equilibration.[19] The nearly identical crystallization[18,19] and the consistent obtained cosmic-ray exposure ages[18–20] in poikilitic shergottites indicate a common original source on Mars, probably ejected from the planet in the same impact and fell to the Earth as separate falls.

This meteorite has been analyzed in several works and their results were summarized in the NASA report on NWA 1950.[21] Some of those works used Raman spectroscopy, and the interpretation of the Raman information evoke the high temperatures and pressures experienced by the meteorite during impact ejection to account for shifts in the Raman spectrum. Shock effects including the transformation of plagioclase to maskelynite (with anorthite being 40%–57%[16]), the formation of planar fractures, and development of strong mosaicism in olivine and strong mosaicism and mechanical twinning in pyroxene, constrain the bulk shock pressure to have been ≥35 GPa but less than 45 GPa. Local shock melting requires a minimum temperature of 1750°C. Magnesian olivine, high-Ca pyroxene, and chromite have crystallized from shock melt, embedded in basaltic glass.[19,22,23] Van de Moortèle et al.[23,24] made a specific characterization of the olivines present in the NWA 1950. In the first part of the work,[24] they concluded that the shock conditions were not sufficient to cause the melting or the transformation of the olivines into their high-pressure polymorphs. They related the dark color of the olivines to the presence of Fe_xNi_y metallic nanoparticles formed during the shock.[24] However, in the second part of the work,[23] Van de Moortèle et al. attributed the small iron nanoparticles in NWA 1950 olivine to a subsolidus transformation of an originally homogeneous magmatic olivine through a shock-induced reduction process. The broad bands in the Raman spectrum of NWA 1950 in the 600–750 cm^{-1} range were attributed to the formation of a new orthosilicate polymorph that formed metastably during shock and was preserved.[23] This last observation agrees with the previous work of Gillet et al.,[16] where some Raman spectra of distorted olivines were also observed. Those spectra consisted of broad main olivine bands and an additional band around 750 cm^{-1}, suggesting the local formation of Si-O-Si bridges. Those bridges are present in $(Mg,Fe)_2SiO_4$-wadsleyite, the high-pressure polymorph of olivine.[16] Shock metamorphism is a notorious heterogeneous process.[25] Therefore, the documented nanoparticles in olivine and the metastable

transition may be expected to vary between samples of NWA 1950.

This work aims to be an improvement of the previously presented non-destructive analytical methodology based also in high-resolution confocal Raman microscopy (single point and imaging analyses) and μED-XRF (imaging analysis). However, in this case, we focus on the Raman imaging analyses. In our previous work,[14] Raman imaging was only used for describing very small and specific micrometric areas that were selected according to the possible interest based on previous single-point Raman results. However, in this case, Raman image is also used to characterize the main mineralogical matrix of the meteorite as the starting characterization point in the same way that the μED-XRF is used in the elemental level. In addition, we added scanning electron spectroscopy coupled to an energy dispersive spectrometer (SEM-EDS) as a complementary elemental characterization of the meteorite to the one previously performed[14] based only on μED-XRF. The SEM-EDS characterization was developed without metallizing the surface of the meteorite to completely preserve the non-destructive nature of the methodology. Finally, in this case, we also tried to describe the degradation reactions of some of the mineral phases on the NWA 1950 based on the identification of different compounds at the same time in the same measuring spot. This measuring spot varies between 1.2 and 2.4 μm depending on the employed objective (100X, 50X, or 20X) for the 785 nm laser of the high-resolution confocal Raman spectrometer used.

2 | MATERIALS AND METHODS

2.1 | Sample description

The NWA 1950 elemental and molecular characterization was performed on a fragment of 0.081 g with both faces of the fragment polished. The characterized fragment is around 6 × 4 cm (Figure S1), which is in the order of the size of the expected returned samples. The returned samples sizes will depend on the nature of the sample collected and thus in the method used to collect them. These samples include interior rock cores, which are expected to be of 1.3 cm diameter with depth varying up to 7.6 cm, loose regolith samples (~8 cm^3), and witness materials.[3] To the naked eye, two main phases, one darker and another one yellowish, can be appreciated in both faces (Figure S1).

According to the description in the Meteoritical Bulletin, the NWA 1950 consists mainly of olivine, $(Mg,Fe)_2SiO_4$ (~55%), high and low Ca pyroxenes, (Ca, Mg, Fe, Mn, Na, and Li) (Al, Mg, Fe, Mn, Cr, Sc, and Ti)

$(Si, Al)_2O_6$ (∼35%), and plagioclase glass (i.e., maskelynite $(Na,Ca)(Si,Al)_3O_8$, a shock-produced glass of plagioclase composition) (∼8%). Other minor minerals such as phosphates in form of merrillite $(Ca_9NaMg[PO_4]_7)$, sulfides as phyrrhotite, $Fe_{(1-x)}S$, chromites $(FeCr_2O_4)$, and spinels $(MgAl_2O_4)$ as inclusions in olivines and pyroxenes are also present.[15] Other characterization studies collected on the NASA report[21] also identified calcite $(CaCO_3)$ and ilmenite $(FeTiO_3)$.

2.2 | Instrumentation

2.2.1 | Raman spectroscopy

The molecular analyses on the NWA 1950 were performed using high-resolution micro-Raman spectroscopy in both single point and spectral imaging modes. Both modes are implemented in the inVia confocal micro-Raman instrument (Renishaw, UK), provided with 785 and 532 nm excitation lasers and a Peltier-cooled charge-coupled device detector $(-70°C)$. The instrument is coupled to a Leica DMLM microscope (Bradford, UK), implementing a Prior Scientific motorized XYZ positioning stage and equipped with a micro-camera for searching the points/areas of interest. For visualization and focusing, 5X N PLAN (0.12 aperture) and 20X N PLAN EPI (0.40 aperture) lenses were used. The spectra were acquired using a 50X N PLAN (0.75 aperture, lateral resolution of 2 μm, and spot size of 2 μm) long-range objective and in some cases using the 20X PLAN EPI (0.40 aperture, lateral resolution of 5 μm, and spot size of 5 μm). The power applied was set at the source at a maximum of 50 mW, whereas on the sample was always less than 20 mW. The spectra were mainly acquired in the range of 100–1400 cm^{-1}, accumulating several scans from each spectrum and modifying the measuring time of each scan in a range from 5 to 20 s to improve the signal-to-noise ratio, and different scans were taken when noise was needed to be reduced in the spectra. The diffraction grating has 1800 lines/mm, giving an average spectral resolution of 1 cm^{-1}, being around 0.8 cm^{-1} for the lowest wavenumbers.

The Raman chemical images were obtained with the same spectrometer using the high-resolution StreamLine technology (Renishaw). The inVia's motorized microscope stage moves the sample beneath the lens so that the line is rastered across the region of interest. Data are swept synchronously across the detector as the line moves across the sample and are read out continuously. In this case, both surfaces of the meteorite were completely characterized. The measuring conditions employed were 20 s of exposure time using the 785 nm laser (a reduced power at a maximum of 50 mW at the source and less than 20 mW on the sample was always used), 20 μm step size, and the 20X objective. The baseline was subtracted in the collected spectra and the cosmic rays were removed when present. The distribution images for each compound were created after selecting the corresponding wavenumber range of the main band for each detected mineral. Finally, the relative intensity of that band in each measurement point (represented as a pixel in the image) is shown on the distribution maps.

The spectrometer was daily calibrated using the 520.5 cm^{-1} silicon line. Data acquisition and treatment were carried out by the Wire 4.2 software package of Renishaw. The results were interpreted by comparing the collected Raman spectra with Raman spectra of pure standard compounds of the e-VISARCH and e-VISART Raman spectra databases,[26] with the RRUFF database[27] and bibliography.

2.2.2 | Energy dispersive X-ray fluorescence

The elemental characterization of the NWA 1950 meteorite was performed using both the single point analysis and the hyper map capabilities of the μED-XRF spectrometer M4 Tornado (Bruker Nano GmbH, Berlin, Germany). The instrument is equipped with two Rh tubes powered by a low-power HV generator and cooled by air. The tube used for this research can work at a maximum voltage and current of 50 kV and 700 μA, respectively. This tube is connected to a mechanic collimation system, which allows to focus the X-ray beam into a measuring spot size of 1 mm. The second tube can work at a voltage between 10 and 50 kV and at a varying intensity between 100 and 600 μA. This tube is connected to a polycapillary focusing optics system. The micrometric lateral resolution of the instrument is performed by a polycapillary focusing optics and the spot size varies as a function of the energy being 17 μm at 2.3 KeV and 32 μm at 18.3 KeV. These small lateral resolutions allow to obtain the elemental distribution on samples of small sizes as the piece of the NWA 1950 studied in this work. The focusing process is supported by two video microscopes, the first explores the sample under a low magnification (1 cm^2 area), whereas the second performs the final focusing (1 mm^2 area) where the analysis is carried out. The instrument was used under vacuum (20 mbar) to enhance the detection of the lightest elements $(Z < 16)$. To achieve the vacuum in the sample chamber, a diaphragm pump MV 10 N VARIO-B was used. The instrument implements an XFlash silicon drift detector with 30 mm^2 sensitive areas and energy resolution of 145 eV for Mn-K_α. The elemental distribution maps were

obtained after a previous assignation of the elements followed by a deconvolution of the spectra. The distributions of each element were obtained using the relative intensity of the K_α X-ray lines of the detected elements. This spectrometer was also calibrated every day using the K_α line of Zr before each measuring session, and the data were treated using the software M4 TORNADO.

2.2.3 | Scanning electron microscopy coupled to energy dispersive detector

The elemental characterization of the meteorite was complemented with a scanning electron microscope JEOL JSM-7000-F (JEOL, Tokio, Japan) coupled to an energy dispersive X-ray detector (Oxford instruments INCA, Energy 350, Oxfordshire, UK). The working voltage of the instrument can vary from 0.5 kV to 30 kV. If the employed voltage is 1 kV, the obtained resolution is 3 nm; if the voltage is increased to 30 kV, the obtained resolution decreases up to 1.2 nm. The microscope allows to focus from 25X to 1,000,000X. The vacuum achieved in this system is not as low as in more modern devices and usually requires the metallization of the sample if the sample is not conductive. In this case, probably because of the great amount of iron in the NWA 1950,[15] the meteorite was conductive enough to obtain good quality images as well as to perform the elemental characterization of the previously selected points under the microscope without the need of covering its surface with carbon or other metals.

3 | RESULTS AND DISCUSION

3.1 | Characterization of olivines

Olivines [$(Mg,Fe)_2SiO_4$] are one of the main components of the igneous lithology of NWA 1950. When using Raman microscopy for olivine characterization, this mineral presents two diagnostic main bands and the position of these bands varies depending on the Fe/Mg proportion of the mineral.[28] Fayalite (Fa, 100% Fe olivine) presents these bands at 817 and 840 cm^{-1}, whereas forsterite (Fo, 100% Mg) presents its bands at 826 and 858 cm^{-1}.[29] The different Fa/Fo solid solutions of the olivines present in the NWA 1950 were obtained according to a previous developed Raman methodology in our group,[30] varying from 60% to 77% of Mg (Figure 1a–e). This observation agrees with the Fo_{75} to Fo_{71} measured by Gillet et al.[16] using electron microprobe, as well as with the Fo_{66} to Fo_{75} observed by Van de Moortèle et al.[24] in their

specific study for olivine characterization in the NWA 1950 by means of transmission electron microscopy-energy dispersive X-ray spectroscopy. This olivine compositional range is characteristic of igneous lithologies as the one of NWA 1950. Olivines that have crystallized from shock melt are distinctly more magnesian (Fo_{78-87}) than those in poikilitic or non-poikilitic igneous lithologies.[22]

The olivine with the lowest Mg content (60%) corresponds to the spectrum showed in Figure 1a, whose main bands appear at 820 and 849 cm^{-1}. The other olivines found in this work can be classified into three different groups according to the three different Mg% ranges obtained: Group (1) olivines with a Mg content between 63.4–64.6% (e.g., Figure 1b, an olivine with the main bands at 820 and 850 cm^{-1}); (2) olivines with a Mg content between 67.9 and 70.6% (e.g., Figure 1c and d, olivines with the main bands at 820 and 851 cm^{-1} and at 821 and 851 cm^{-1}); and (3) olivines with a Mg content between 73.7 and 77.1% (Figure 1e, an example of an olivine with the main bands at 821 and 852 cm^{-1}).

This variation in the Fe/Mg content may be explained because of alterations of the original olivine (probably the ones with the lowest Mg%, ~60%) as their degradation implies Fe loss because of the formation of other ferrous and ferric compounds and, thus, an enrichment in their Mg content. In fact, Van der Moortèle et al.[24] documented the formation of iron nanoparticles in the NWA 1950 olivines. In our present work, additional bands in the Raman spectrum acquired from those olivine grains with the lowest Mg% suggest the presence of another mineral.

In the first group of olivines with a 63.4–64.6% of Mg, hematite can also be identified together with the olivine bands in most of the Raman spectra (Figure 1b). The hematite that appears together with the olivine presents its characteristic bands at 224, 290, 406, 495, and 608 cm^{-1} (Figure 1b), shifted to lower wavenumbers than the reported hematite bands at 227, 293, 412, 497 and 610 cm^{-1} for standard Earth conditions.[31,32] Taking into account that the mean resolution of the Raman spectrometer is 1 cm^{-1} and even lower in the range of the hematite bands, ~0.8 cm^{-1}, we can ascertain that there is a shift in the position of the bands of hematite. This shift to lower wavenumbers occurs due to a temperature increase[31] that may have happened during the impact ejection from Mars or during the entrance to the terrestrial atmosphere. It must be also highlighted that the very wide band at 495 cm^{-1} (Figure 1b) may also be encompassing the signal of vitreous silica, in agreement with the high temperature event experienced by the meteorite. The alteration of the original olivine ($Fo_{60}Fa_{40}$) to the olivine with a 63.4–64.6% of Mg can be explained by the
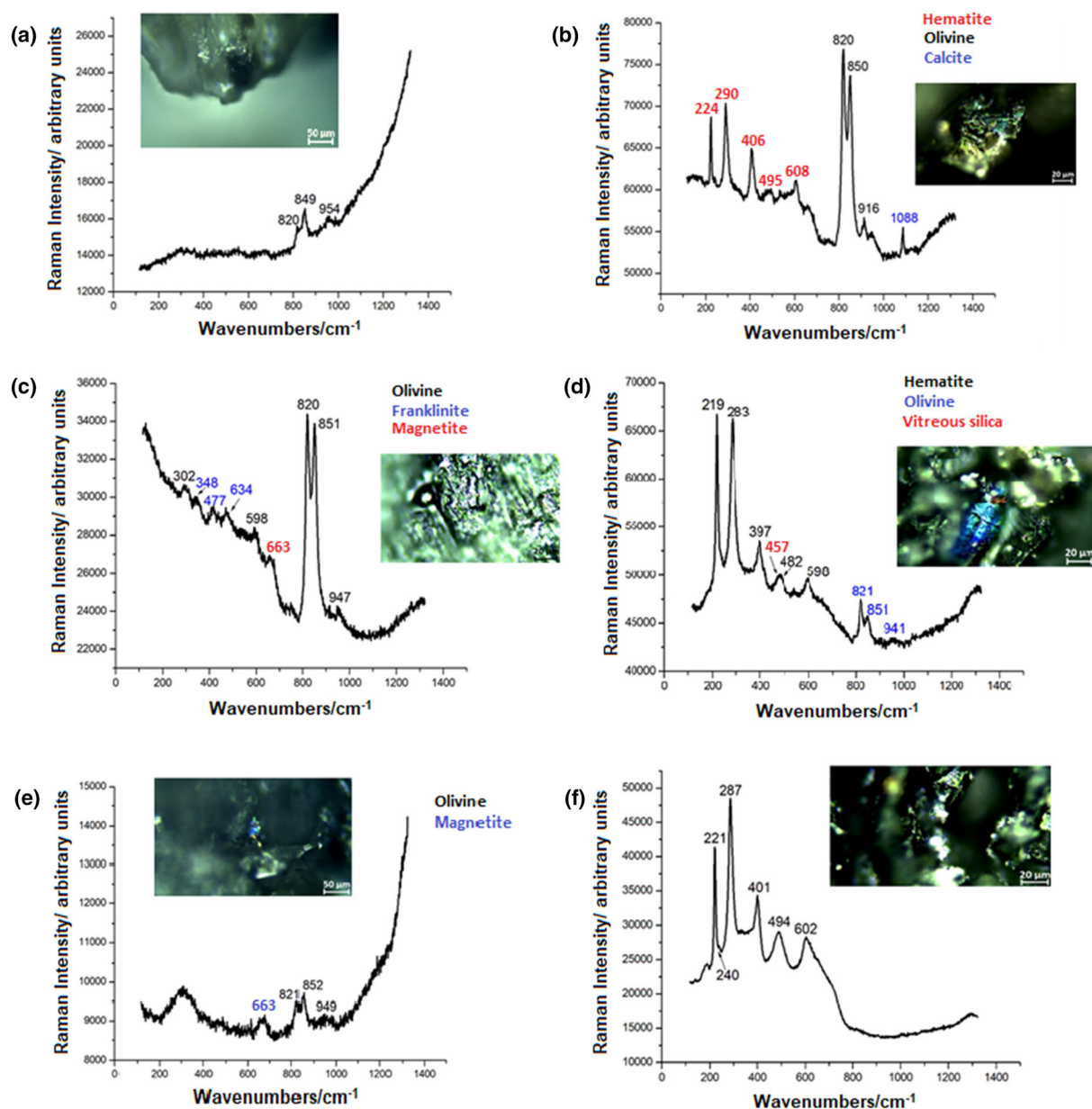
FIGURE 1 Raman spectra showing (a) olivine 60% Mg; (b) olivine 63.4–64.6% Mg, hematite (Fe_2O_3), and calcite ($CaCO_3$); (c) olivine 67.9–70.6% Mg, magnetite (Fe_3O_4), and franklinite ($(Fe,Mn)_3O_4$); (d) olivine 67.9–70.6% Mg, hematite (Fe_2O_3), and vitreous silica (SiO_2); (e) olivine 73.7–77.1% Mg and magnetite (Fe_3O_4); and (f) hematite Fe_2O_3 [Colour figure can be viewed at wileyonlinelibrary.com]

partial oxidation of Fayalite giving rise to hematite (Fe_2O_3) and silica (SiO_2) according to the reaction equation (1).

$$2\,Fe_2SiO_4 + O_2 \rightarrow 2\,Fe_2O_3 + 2\,SiO_2 \qquad (Eq1)$$
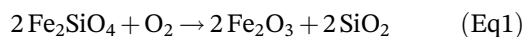
The oxidation of fayalite to hematite at high temperatures has already been demonstrated in other studies.[33] As a consequence of the oxidation of the fayalite, the olivine decreases its fayalite content and increases the forsterite one. Because of the high temperatures needed for the

oxidation of the olivine, to the shifted bands of the hematite to lower wavenumbers and to the band of vitreous silica, it can be ascertained that this degradation of the olivine took place on the ejection event or during its entrance to the Earth atmosphere. Other hematite Raman spectra were also obtained (Figure 1f) focusing on specific hematite grains, and their Raman bands appeared once again shifted to lower wavenumbers than usual as the effect of the temperature suffered by this meteorite.

In the case of the second group of olivines with a 67.9–70.6% of Mg, their Raman bands appeared together

with magnetite ($Fe^{2+}Fe^{3+}_2O_4/Fe_3O_4$) (Figure 1c) and also with hematite (Figure 1d) in most of the collected spectra for that group. In Figure 1c, the band at 663 cm^{-1} shows the presence of magnetite.[31,34,35] In this case, the oxidation of the fayalite also gives rise to the formation of magnetite according to the reaction equation (2):

$$3\,Fe_2SiO_4 + O_2 \rightarrow 2\,Fe_3O_4 + 3\,SiO_2 \qquad (Eq2)$$
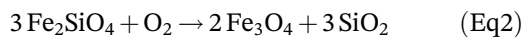
The oxidation of fayalite to magnetite at high temperatures has also been proved previously.[33] This reaction is written for pure iron fayalite; however, in nature, Fe may be substituted by Mn in this type of minerals.[36] If there is a small amount of Mn, as detected by XRF in areas where iron is abundant, then the oxidation of that Fe could lead to the formation of the mineral franklinite ($(Fe,Mn,Zn)^{2+}(Fe,Mn)^{3+}_2O_4/(Fe,Mn)_3O_4$), which can be described as magnetite with an important Mn content. This mineral was also observed (Figure 1c) with its bands at 634, 477, and 348 cm^{-1} together with the magnetite in the degradation of the olivines present in NWA 1950. These bands are also shifted in comparison to the bands for the non-impacted franklinite at 638, 470, and 343 cm^{-1}.[37] These shifted bands may indicate that franklinite was also subjected to a mixture of high pressure and temperature and therefore suggesting its Martian origin. The olivines with a 67.9–70.6% of Mg were also found together with hematite because of the oxidation of fayalite according to reaction equation (1) (Figure 1d). In this case, the broader band obtained at 470 cm^{-1} was subjected to deconvolution obtaining a band with its maximum at 457 cm^{-1} because of the vitreous silica, and a second band at 482 cm^{-1} because of the secondary band of the hematite (Figure 1d). The bands of this hematite are shifted to even lower wavenumbers than the previous ones. Both, the presence of vitreous silica and shifted bands of hematite (219, 283, 397, 482, and 598 cm^{-1}) show again the effect of the high temperatures on the altered olivines of the meteorite before the meteorite arrived to the surface of the Earth.

Finally, the third group of olivines with 73.7–77.1% of Mg are the ones with the lowest Fe content and therefore the most altered ones. These olivines were found together with only magnetite (Figure 1e) but never with hematite, suggesting an alteration because of to the oxidation of fayalite according to the reaction equation (2).

However, metallic iron nanoparticles have also been detected by high-resolution transmission electron microscopy (HRTEM) in the work by Van de Moortèle et al.[24] Metallic iron cannot be detected by Raman spectroscopy, thus together with the remaining olivine, the magnetite and the silica, iron nanoparticles can be also present in the same spot area of analysis. In consequence, other possible alteration reaction that could have taken place is the disproportionation of Fe (II) in the olivine, induced by the shock pressure,[38] according to the reaction equation (3):

$$2\,(FeO)_2.SiO_2 \rightarrow Fe^{(0)} + Fe_3O_4 + 2\,SiO_2 \qquad (Eq3)$$
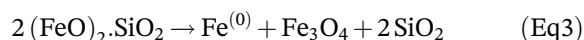
This other alteration reaction could explain the simultaneous presence of all the minerals detected by Raman spectroscopy plus the metallic iron detected by HRTEM in the work of Van de Moortèle et al.[24] In all the situations, the minerals should be considered from Martian alteration processes because of the shifts found in the iron oxides.

Of course, it is not disposable a terrestrial oxidation of the Fe(0) nanoparticles also to justify the presence of hematite in the meteorite but goethite is not present in the meteorite, being this a very stable phase that would be expected to be found in this case. This fact, together with the shift observed for the iron oxides makes more probable the Martian origin of the iron oxides.

The distribution of the olivines was analyzed by µED-XRF and Raman (Figure 2) imaging analysis in both faces of the meteorite (Faces A and B). In Figure 2a1 and 2b1, the Fe distribution obtained by µED-XRF in each face (A and B), respectively, is shown. In Figure 2a2 and 2b2, the Mg distribution in each Face A and B, respectively, is shown. Olivines appear as the more intense big grains where Fe and Mg are coincident. The intensity in the µED-XRF map of Fe is especially higher in the grains of olivines and, therefore, the big grains are better appreciated because of the higher proportion of Fe in the olivines with respect to the Fe content in the rest of the mineral phases that compose the matrix of the meteorite. This observation was corroborated by the Raman imaging analysis performed over a big part of each Face A and B (Figure 2. a3, and b3). The Raman surface analyzed is marked over the iron µED-XRF map distributions (Figure 2a1 and b1) with a yellow square. The distribution of the olivines in the meteorite (Figure 2a3) was performed by representing the distribution of the signal obtained in the range 806–865 cm^{-1} for both faces (Figure 2b3), encompassing the two main bands of olivines. As can be appreciated, the olivine grains distinguished by Raman imaging on each face correspond also with the abovementioned olivine grains showed based on Fe and Mg distributions by µED-XRF imaging. One of the advantages of the Raman imaging analysis is its capability to obtain the distribution of the mineral
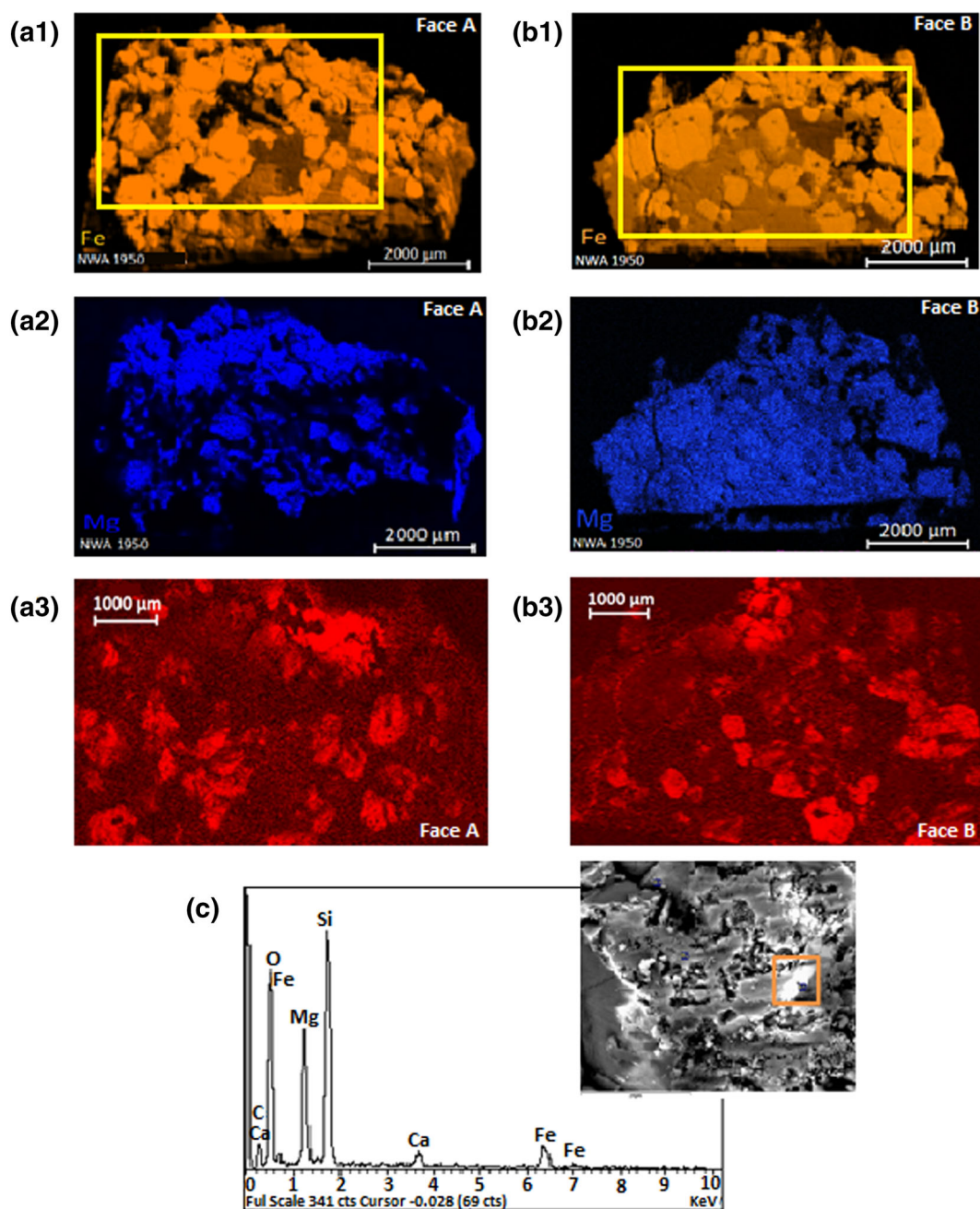
FIGURE 2 (a1) µED-XRF distribution of Fe in Face A, (b1) µED-XRF distribution of Fe in Face B, (a2) µED-XRF distribution of Mg in Face A, (b2) µED-XRF distribution of Mg in Face B, (a3) Raman distribution for olivines in Face A, (b3) Raman distribution for olivines in Face B, and (c) SEM-EDS image and analysis of an olivine crystal [Colour figure can be viewed at wileyonlinelibrary.com]

phases. In this case, it can be appreciated how the olivines in Face A (Figure 2a1, a2, and a3) and in Face B (Figure 2b1, b2, and b3) are distributed all along both surfaces in a similar way.

The olivine crystals were also measured by means of SEM-EDS. In Figure 2c, a SEM-EDS image and spectrum showing the elemental composition of an olivine crystal is shown. Note that the calcium observed in the EDS spectrum probably is because of an adjacent pyroxene.

3.2 | Characterization of pyroxenes

Pyroxenes together with olivines are the main mineral phases composing the matrix of the NWA 1950 meteorite. The general formula of a pyroxene could be written as (Ca, Mg, Fe, Mn, Na, Li) (Al, Mg, Fe, Mn, Cr, Sc, Ti) (Si, Al)$_2$O$_6$. In this meteorite, different pyroxenes have been identified by Raman spectroscopy. On the one hand, and in agreement with the petrological characterization of Gillet et al.,[16] low-Ca pyroxenes (Mg and Fe rich
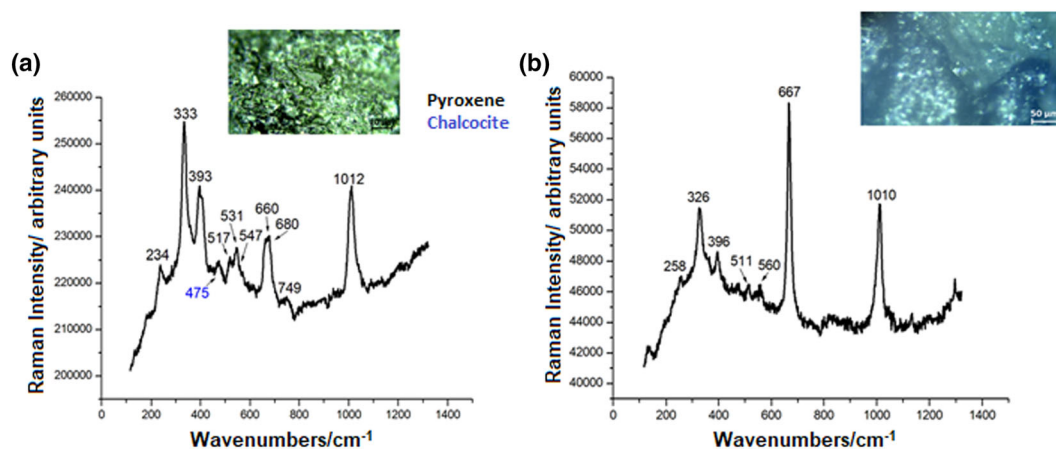
FIGURE 3 (a) Raman spectrum of an orthopyroxene (low-Ca pyroxene) similar to $En_{87}Fs_{13}$ together with the main Raman band of chalcocite (Cu_2S). (b) Raman spectrum of the clinopyroxene (high-Ca pyroxene) similar to $En_{45}Fs_{04}Wo_{50}$ [Colour figure can be viewed at wileyonlinelibrary.com]

pyroxenes) were identified. In Figure 3a, a Raman spectrum of a low-Ca pyroxene is shown. In this case, the obtained spectrum presents a very similar Raman spectrum to the one of the pyroxene like $En_{87}Fs_{13}$, an orthopyroxene with a composition of 87% enstatite (En, $MgSiO_3$) and 13% ferrosilite (Fe, $FeSiO_3$).[38]

On the other hand, Raman spectra corresponding with clinopyroxenes were also detected as described also by Gillet et al.[16] In the mentioned work, the clinopyroxene was identified as the high-Ca clinopyroxene augite ($CaMgFe)_2(SiAl)_2O_6$ group (e.g., $En_{71.9}Wo_{55}Fs_{22.7}$). In our case, the best Raman spectrum obtained for the clinopyroxenes is shown in Figure 3b, and the features in its Raman spectrum matches very well with the one with a composition $En_{45}Fs_{04}Wo_{50}$.[39] This pyroxene, apart from enstatite and ferrosilite, contains a wollastonite component (Wo, $CaSiO_3$), and it belongs to the group of the high-Ca pyroxenes[39,40] and was not previously reported by the petrographic analysis performed by Gillet et al.[16]

The μED-XRF and Raman imaging analysis showing the distribution of the pyroxenes in both faces of the NWA 1950 are collected in Figure 4. The μED-XRF distributions were drawn according to the intensity of the K_α line of the elements (Figure 4a1 and b1), whereas the Raman distributions (Figure 4a2 and b2) have been represented according to the intensity for the signal in the range 644–704 cm^{-1} for both faces. These ranges covered in both analyses the range where the main and common signal for all kind of pyroxenes appears. The slightly smaller analyzed surface by means of Raman microscopy is indicated with yellow squares over the complete surface analysis performed by μED-XRF.

Iron is a common element for olivines and pyroxenes, so it is present all along the surface of the meteorite. However, as Fe is present in olivines at a higher Fe proportion than in pyroxenes, the olivine grains appear with higher Fe intensity, and therefore, the lighter color in the Fe distribution corresponds to the presence of the pyroxenes in the meteorite (Figure 4a1 Fe and b1 Fe). These Fe distributions and the Raman distribution (Figure 4a2 and b2) for the pyroxenes show how they form part of the main matrix surrounding the olivine crystals (with higher Fe intensity in the elemental distributions and with no signal in the selected range for the Raman distributions).

In this case, the elemental distribution allows to distinguish between different kinds of pyroxenes. The zones where no K and Al are observed and the signal where Ca is low correspond to the low-Ca pyroxenes, as it can be the orthopyroxene detected by Raman. The zones with a higher intensity of Ca signal and matching the distribution of Al could be because of the high-Ca pyroxene augite detected as the high-Ca pyroxene type by Gillet et al.[16] or to the diopside high-Ca pyroxene detected in our work. Different pyroxenes can be distinguished based on a higher or lower Fe/Mg ratio.

3.3 | Shocked plagioclase

As stated before, plagioclase is the third main mineral in the NWA 1950 meteorite, with a relative abundance around 8%. Gillet et al.[16] reported plagioclase as shocked maskelynite with anorthite in the 40–57% range. Shocked plagioclases are difficult to detect by Raman
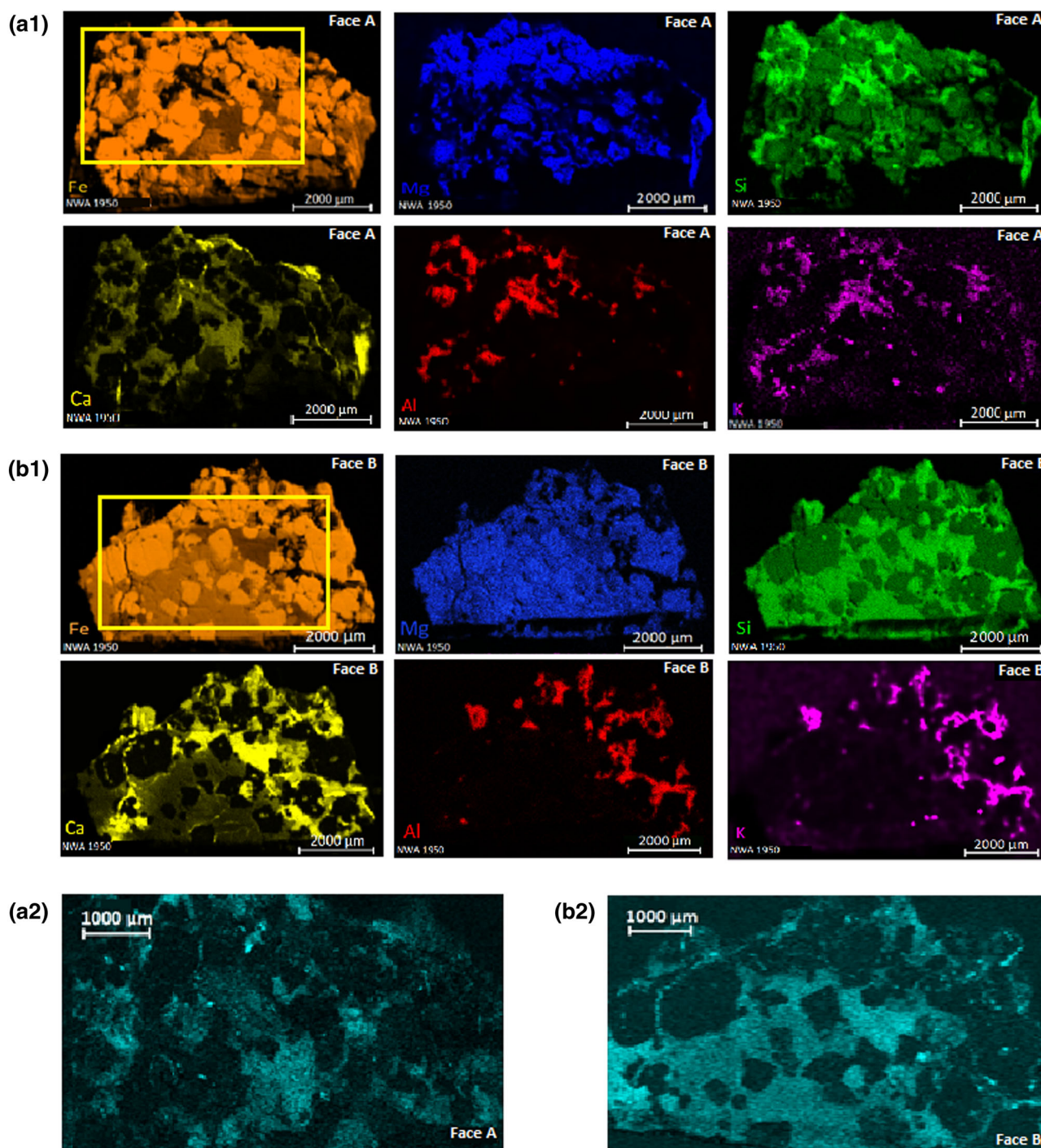
FIGURE 4 (a1) µED-XRF image distributions of the elements composing the pyroxenes (Fe, Mg, Si, Ca, Al, K) in Face A of the meteorite. (b1) µED-XRF image distributions of the elements composing the pyroxenes (Fe, Mg, Si, Ca, Al, K) in Face B of the meteorite. (a2) Raman distribution for pyroxenes in Face A of the meteorite. (b2) Raman distribution for pyroxenes in Face B of the meteorite [Colour figure can be viewed at wileyonlinelibrary.com]

spectroscopy,[41] especially when the shocked pressure has been greater than 35 GPa as reported for this meteorite.[21] Our Raman observations confirm the presence of weak and broad features in the expected range for maskelynite (see Figure 7), containing in some cases the characteristic bands at 508 cm^{-1} for glassy anorthite as reported by Sharma et al.[42] This finding of glassy anorthite is in agreement with the suggestion of Gillet et al.[16]
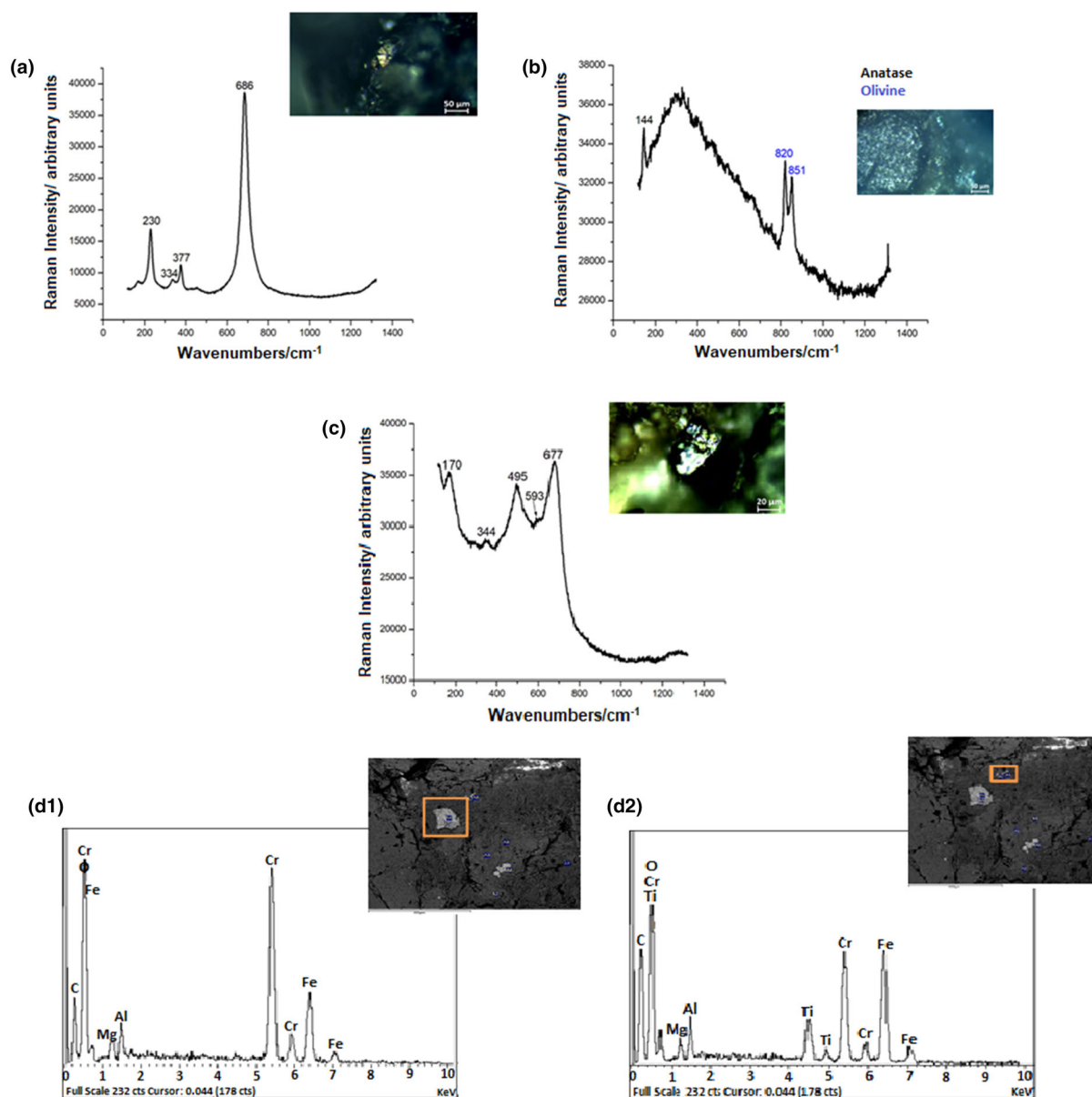
FIGURE 5 (a) Raman spectrum for ilmenite (FeTiO$_3$), (b) Raman spectrum of anatase (TiO$_2$), (c) Raman spectrum for chromites (FeCr$_2$O$_4$), and (d1 and d2) SEM-EDS for two different chromites [Colour figure can be viewed at wileyonlinelibrary.com]

3.4 | Ilmenite and anatase

Ilmenite (FeTiO$_3$) was found as an accessory phase mineral in the non-poikilitic regions of the NWA 1950 as previously described by Gillet et al.[16] and on the NASA report.[21] In Figure 5a, a Raman spectrum obtained over a grain on the meteorite shows the presence of ilmenite at 686, 377, 334, and 230 cm^{-1}. However, the normal Raman signals for ilmenite are expected to be at 681 (A$_g$ν1), 371 (A$_g$ν3), 333 (E$_g$ν3), and 226 (A$_g$ν4) cm^{-1}.[43] When ilmenite is subjected to high pressure, its Raman peaks are shifted to higher wavenumbers. Specifically, the peaks A$_g$ν1, A$_g$ν3, and E$_g$ν3 are shifted linearly with the increase of the pressure, whereas A$_g$ν4 increases in a nonlinear way because of Fermi resonance effects.[43] The changes because of pressure are not completely reversible when ilmenite is back to atmospheric pressure,[43] and the shift observed in our Raman spectra may be because of the incomplete return of an ilmenite, which was once subjected to high pressures. In addition, the meteorite also suffered high temperatures that makes the opposite effect on the peaks, shifting them to lower wavenumbers[44] increases the complexity to understand the changes on the Raman

spectra. However, what is clear is that some changes remained in the spectra we obtained, showing up that this ilmenite is original from Mars and affected by high and/or high temperatures and pressures. Because, if the ilmenite had been formed on the Earth, it would have never suffered these pressure and temperature changes and the Raman spectra would have remained unchanged.

The elemental distributions for Ti and Fe obtained by means of µED-XRF also corroborate the presence of ilmenite. The Ti distribution obtained based on its K_α line (Figure S2) shows the abundant presence of Ti particles in both faces of the meteorite. In this case, the comparison with the Fe distribution is not straightforward because Fe is present all over the meteorite because of its presence in olivines and pyroxenes. In any case, where Ti is present, Fe is present as well, which is in agreement with the presence of ilmenite.

Regarding TiO_2, depending on the temperature, it can be found as different polymorphs. In this meteorite, the TiO_2 identified by Raman spectroscopy was the anatase polymorph (Figure 5b). The presence of the anatase polymorph is indicative that the oxidation reaction of ilmenite took place below 400°C, as anatase is the low temperature polymorph. Therefore, the ilmenite oxidation occurred while the meteorite was on the Earth's surface. The presence of anatase has not been reported yet for the NWA 1950, only Gillet et al.[16] identified the presence of titanium oxide (TiO_2) by means of electron microprobe but the polymorph was not identified, as this technique can only quantify the chemical composition but cannot determine its structure. Ilmenite can be oxidized to TiO_2 and hematite (Fe_2O_3) according to the reaction equation (4)[45]:

$$4\,FeTiO_3 + O_2 \rightarrow 2\,Fe_2O_3 + 4\,TiO_2 \qquad (eq4)$$
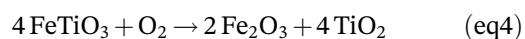
3.5 | Chromites

Chromites have already been described as a minor phase in the Meteoritical Bulletin[15] and also in the characterization performed by Gillet et al.[16] In this work, we were also able to identify the chromites by means of Raman spectroscopy. In Figure 5c, a Raman spectrum of a chromite is displayed with the main bands at 677, 593, and 495 cm^{-1}. According to the Raman study of different spinel structure minerals performed by D'Ippolito et al.,[46] the Raman spectra obtained in this work could correspond to iron chromite ($FeCr_2O_4$), whose main Raman bands appear at 674, 591, and 493 cm^{-1}.[46] The main peak assigned to the vibration mode A_{1g} is known to vary its wavenumber position from the $\sim$674 cm^{-1} in the pure synthetic $FeCr_2O_4$ to higher wavenumbers up to 690 cm^{-1} in natural chromites.[46] This difference can be because of chemical composition variations in the natural ones. For example, Lenaz and Lughi[47] showed that there is a systematic shift of this peak with the increase of the chromite end-member in the $MgCr_2O_4$- $FeCr_2O_4$ solid solution. Another study performed by Wang et al.[48] described a systematic shift to higher wavenumbers and a broadening of the main peak (A_{1g}) when increasing the Al content. Therefore, the slight variation observed in the natural chromites in the NWA 1950 from the pure $FeCr_2O_4$ reported by D'Ippolito[46] can be because of the presence of Mg and Al. This evidence would be in agreement with the observations of Gillet et al.[16] that described the chromites as strongly zoned with compositions varying from Cr-rich cores to Fe/Al/Ti-rich rims. We were also able to identify the chromite particles under the SEM-EDS; in all the elemental spectra obtained for these particles, the chromites presented slight amounts of Mg and Al (Figure 5d1 and d2) corroborating that the presence of these elements was the reason of the shift in the Raman spectra. In addition, two different types of chromites were distinguished in our work according to the presence or absence of Ti (Figure 5d1 and d2).

3.6 | Merrillite

Merrillite ($Ca_9NaMg[PO_4]_7$) is another mineral phase identified in the NWA 1950[15,16] as an accessory mineral. We have also been able to identify this mineral by Raman spectroscopy. In Figure 6a0, one of the spectra obtained for merrillite is displayed where the two main bands for this mineral can be clearly seen at 958 and 975 cm^{-1} in concordance with the literature.[49] Moreover, we were also able to find the distribution of merrillite in both faces of the meteorite, by means of both µED-XRF and µ-Raman imaging. In Figure 6a1 and b1, the elemental distributions of Ca (yellow) and P (red) are displayed together for both faces of the meteorite, Faces A and B, respectively. In addition, Figure 6a2 and b2 shows the Raman distributions obtained for the Raman ranges 954–981 cm^{-1} (Face A) and 950–982 cm^{-1} (Face B) containing the two main bands of merrillite. If we compare the coincident elemental mappings of Ca and P (in orange) with the Raman distribution of merrillite (green hotspots), the same distributions and therefore the presence in both cases of merrillite can be clearly
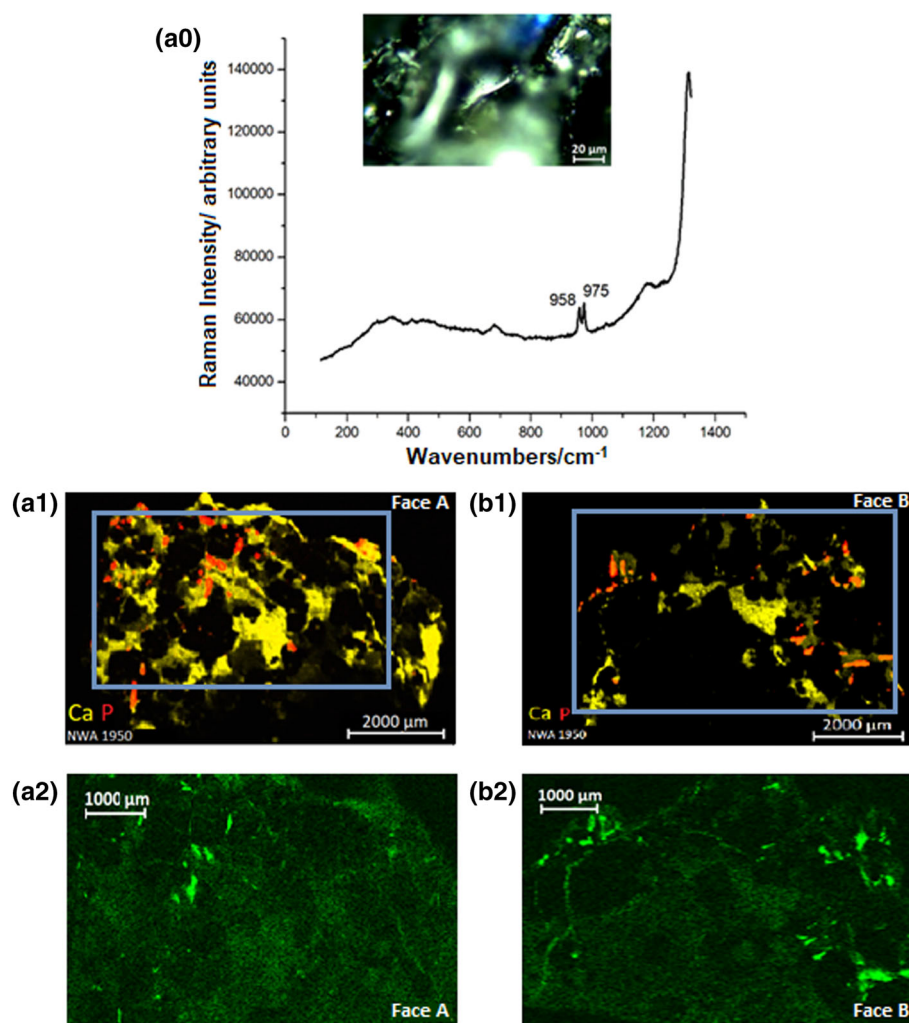
FIGURE 6 (a0) Raman spectrum for merrillite (Ca$_9$NaMg[PO$_4$]$_7$), (a1) µED-XRF image distributions of the elements composing merrillite (Ca and P) in Face A. (b1) µED-XRF image distributions of the elements composing merrillite (Ca and P) in Face B. (a2) Raman distribution of merrillite in Face A. (b2) Raman distribution of merrillite in Face B [Colour figure can be viewed at wileyonlinelibrary.com]

appreciated. In addition, the distribution of merrillite shows that it is in the form of grains inside the matrix of the meteorite.

3.7 | Calcite

Calcite has also been identified in the NWA 1950 mainly filling a fracture in Face B. Gillet et al.[16] also reported the presence of calcite filling fractures as the only trace of terrestrial weathering in the NWA 1950 meteorite. The terrestrial origin of calcite, formed at atmospheric pressure and temperature, was confirmed because of its main peak at 1086 cm^{-1}[14] was measured in the filling material of fractures in NWA 1950, as shown in Figure 7a. The calcite filling fractures can be seen in Figure 7b (elemental distribution of Ca) and in Figure 7c (Raman image of calcite) where calcite is filling the main fracture in the Face B of the meteorite.

However, we were also able to identify several calcite grains with the main band between 1088 and 1089 cm^{-1}

(see Figure 7d1 and d2). This main band at higher wavenumbers than 1086 cm^{-1} could be because of the presence of Mg, but according to the XRF distribution of Mg, there is no Mg in these grains. The other possible reason for this shift could be because of the pressure and temperature suffered by the meteorite and may suggest the presence of a Martian calcite. The Raman peak position of calcite varies irreversibly when calcite is subjected to high pressures[50] and temperatures.[51] Specifically, the bands of calcite are displaced to higher wavenumbers when calcite is subjected to high pressures.[50] What is more, at pressures above 1.4[50] or 1.7 GPa,[52] CaCO$_3$ suffers an irreversible phase transition to the monoclinic CaCO$_3$-II, which implies a change in the symmetry that leads to a shift above 1090 cm^{-1} for the main band, a splitting of the 712 band into a pair of modes at 715 and 721 cm^{-1} and the appearance of two additional external modes at 133 and 204 cm^{-1}.[52] On the other hand, the effect of temperature in the Raman shifts is not very well defined yet, although it is known that the Raman bands become broader and are shifted to lower wavenumbers
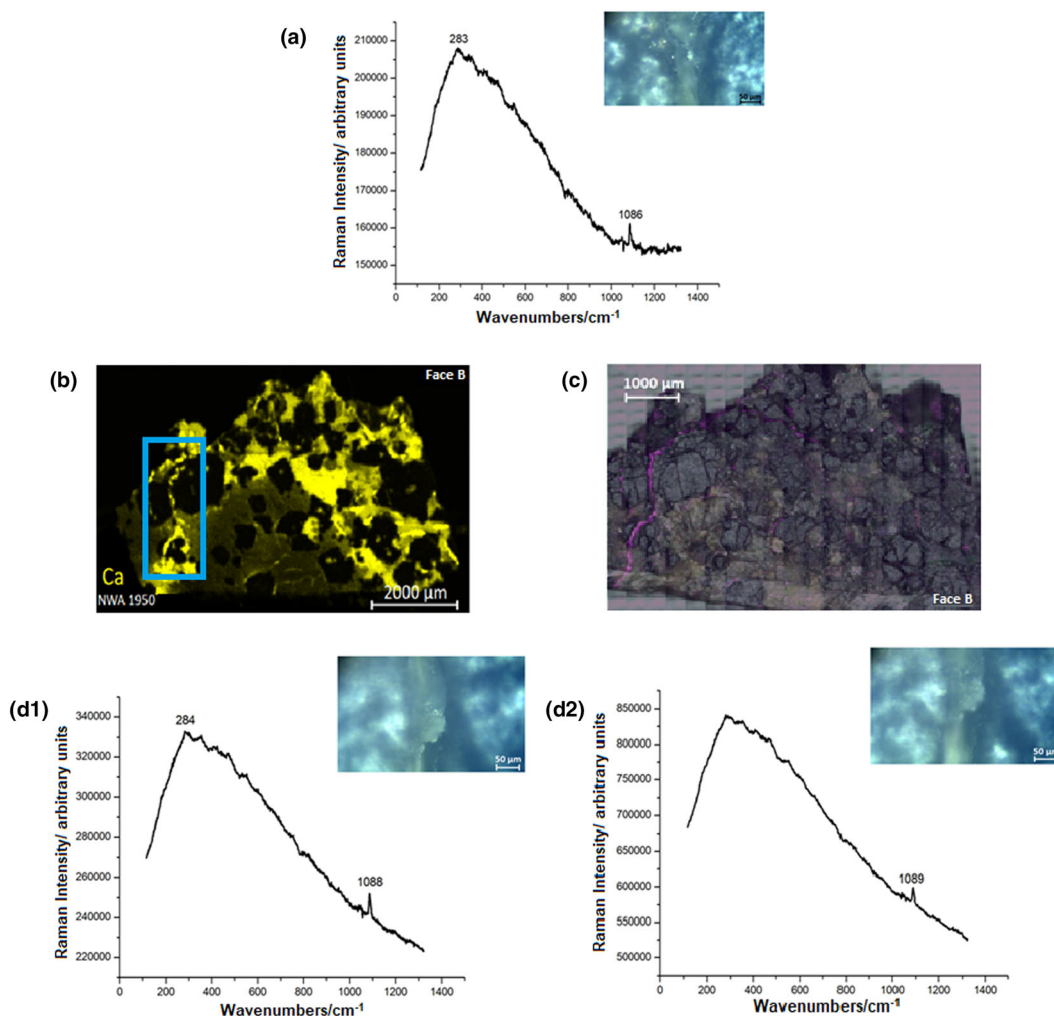
FIGURE 7   (a) Raman spectrum for calcite. (b) μED-XRF image distributions for Ca. (c) Raman distribution for Calcite. (d1 and d2) Raman spectra for shocked calcite grains. The three spectra show the broad weak feature of shocked plagioclases around 508 cm^{-1} [Colour figure can be viewed at wileyonlinelibrary.com]

FIGURE 8   (a) Raman spectrum for acanthite (Ag$_2$S) and (b) SEM-EDS for a particle containing Ag and S. The broad feature around 508 cm^{-1} is consistent with shocked plagioclase [Colour figure can be viewed at wileyonlinelibrary.com]
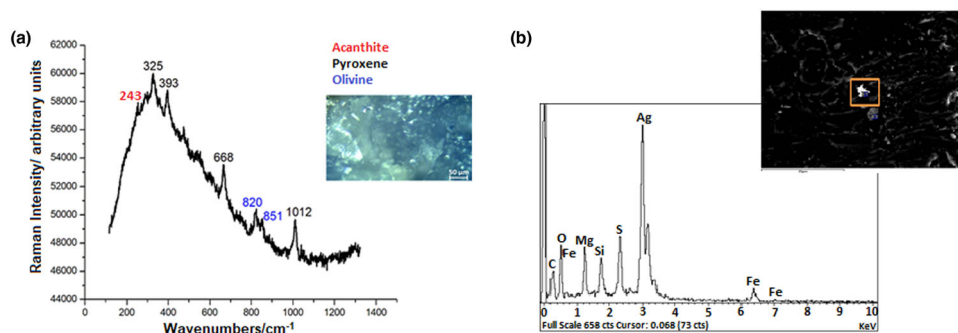
with increasing temperature,[51] especially affecting the bands at low wavenumbers. As seen, the Raman image shows the calcite filling the fractures in the NWA 1950 meteorite (Figure 7d2).

3.8 | Sulfides

Raman microscopy also allowed us to identify different sulfides in the NWA 1950. These sulfides appear as a very

minor phase on the analyzed surface and in the form of very small size grains.

A Raman band identified at 475 cm^{-1} could be assigned to the main band of Chalcocite (Cu_2S)[53] (Figure 3a). As the chalcocite is a minor mineral, we were not able to obtain a spectrum with each secondary bands. However, the presence of this band who may be attributed to the main band of Chalcocite together with the observations previously made by Gillet et al.[16] who described the presence of zones enriched in Cu (up to 11%) within the sulfides makes highly possible the presence of this mineral in the meteorite.

We were also able to identify another sulfide not previously reported for the NWA 1950, the acanthite (Ag_2S) by Raman spectroscopy with its main band at 243 cm^{-1}[54] (Figure 8a). The presence of a silver sulfide was also observed using the SEM-EDS (Figure 8b). As can be appreciated in the SEM image, the silver sulfide is forming a grain inside the matrix of the meteorite, which may be indicative of its Martian origin. In addition, the acanthite is stable under 180°C while at higher temperatures the stable compound is the argentite (α-Ag_2S). If the acanthite was original from Mars, argentite would have been formed because of the high temperatures produced by the ejecting impact and because of the entrance in the terrestrial atmosphere but it would have changed back to acanthite once on the Earth, as this reaction is reversible.[54,55]

4 | CONCLUSIONS

This work presents a non-destructive analytical methodology that could be used as a first characterization for the Martian samples that will be brought to the Earth in the upcoming mission MSR. The analytical methodology has been tested on a fragment of the NWA 1950 meteorite being able to give us a mineralogical characterization of the meteorite providing new information of its original composition and the degradation suffered by this meteorite to the previous studies.[16,17,21,24] This work also shows the advantages and disadvantages that each of the techniques employed has when performing a mineralogical characterization, the information that each one can provide and the importance of combining them.

The analytical methodology described in this work allowed us to characterize the different kind of olivines as in other works and allowing us to describe the oxidation degradations they suffered. The spot size of Raman micro-spectroscopy allowed us to detect in the same spot the original mineral and the alteration product, helping us to understand that the mineral phases found may be related and have a common origin.

Thanks to a previous Raman calibration methodology developed in our group for distinguishing the Fe/Mg ratio of the olivines, we were able to identify different oxidation reactions depending on the %Mg content of the olivine. In addition, the Raman band shifts of the oxidation products, hematite, magnetite, and franklinite indicate that the oxidation reaction of the olivines that we describe in this work was already happening on Mars. Mars atmosphere is an oxidizing atmosphere; even if the main constituents are CO_2, N_2, and Ar, the OH radicals and O atoms produced by photolysis because of the stellar UV radiation result in surface oxidation and the formation of O_2, O_3, and H_2O_2.[56]

It was observed that the selection of a proper objective for the analysis of the surface of this type of sample is critical, because with the selection of a proper objective it was possible to detect original and altered minerals in the same spot, which allows to provide more complete descriptions of the alterations processes that affect the primary minerals. We suggest performing a deep screening of the surface under analysis to match grain sizes with the field of view of the objective. The observation of Raman signals of original and altered minerals is of great importance when thinking about not only characterizing the Martian samples but also about the possibility to search for alteration processes and the evolution of mineral phases that were taking place on Mars.

In the case of pyroxenes, we were able to distinguish between high and low Ca-pyroxenes already detected and also to identify some new ones, as the high-Ca pyroxenes. In this case, we showed one advantage of the µED-XRF over the Raman microscopy and showed the importance of performing it. In this case, the distribution of the elements composing the pyroxenes allowed us to show the distribution of the two kind of pyroxenes, the high and low-Ca ones.

Raman observations have confirmed the presence of shocked plagioclases although their characteristic bands are weak and broad, in agreement with the shocked pressure[21,41] suffered by the NWA 1950 meteorite.

The detection of ilmenite, previously known for this meteorite, was complemented with establishing the Martian origin of this titanium oxide based on the shift of its Raman bands. What is more, the detection of anatase (the presence of TiO_2 was only reported[16] but not the polymorph) is important to understand the processes around the meteorite. As anatase is the low temperature polymorph of TiO_2, we propose that this mineral is coming from the oxidation of ilmenite on Earth. The identification of chromites already stated for this meteorite[15,16] was also complemented. In this case, Raman spectroscopy was able to identify iron

chromites ($FeCr_2O_4$), and the Raman peaks were slightly shifted to the ones observed for pure iron chromite and that was the first sign indicating the possible presence of Mg and Al. However, SEM-EDS was necessary in this case to confirm the presence of Mg and Al in the chromite particles as the µED-XRF image analysis was not useful because Fe, Mg, and Al were present in almost all the matrix of the meteorite. In addition, SEM-EDS showed us the presence of two different chromites based on the presence or absence of Ti on them. In the identification of merrillite, we were able to observe its distribution all over the surface of the meteorite in the µED-XRF with the overlap of Ca and P and in the Raman image based on the main Raman peaks of merrillite. The calcite that filled fractures along the meteorite was confirmed to be of terrestrial weathering origin, whereas different calcite grains were also identified that may be of Martian origin, something not reported until now. Finally, the presence of some sulfides, among them acanthite (Ag_2S) not previously reported, was identified by Raman and SEM-EDS. In this case, probably because of the very small size of the sulfide particles, the obtained Raman spectra were of very poor quality for the identification of the sulfides showing only the main peak with low intensity, and therefore, the identification by SEM/EDS of these particles containing the expected elements was crucial to finally identify them.

The present non-destructive analytical methodology, combining the information from high-resolution Raman imaging, µED-XRF imaging, and SEM/EDS images, has been demonstrated extremely useful to characterize minerals and obtain their distributions on the meteorite surface. Depending on the matching of mineral grains and surrounded areas with the field of view of the used microscopic objectives, several minerals can be identified in the same analysis, allowing us to describe chemical reactions taking place on the minerals. This success suggests the use of this analytical methodology as a first stage for the characterization of samples from the MSR mission. This analytical methodology is also cost effective in comparison to the synchrotron radiation installations, which have been suggested for the preliminary analysis of such samples. In our opinion, synchrotron-based methodologies could be used in a more advanced step of the analysis of the forthcoming Mars samples for specific analysis.

DATA AVAILABILITY STATEMENT
Data available on request from the authors.

ORCID
Leire Coloma https://orcid.org/0000-0002-3739-3296
Cristina García-Florentino https://orcid.org/0000-0002-0329-8012
Jennifer Huidobro https://orcid.org/0000-0001-8302-8583

REFERENCES
[1] https://mars.nasa.gov/news/9029/nasas-perseverance-rover-collects-first-mars-rock-sample/
[2] B. K. Muirhead, A. K. Nicholas, J. Umland, O. Sutherland, S. Vijendran, *Acta Astronaut.* **2020**, *176*, 131.
[3] R. C. Moeller, L. Jandura, K. Rosette, M. Robinson, J. Samuels, M. Silverman, K. Brown, E. Duffy, A. Yazzie, E. Jens, I. Brockie, L. White, Y. Goreva, T. Zorn, A. Okon, J. Lin, M. Frost, C. Collins, J. B. Williams, A. Steltzner, F. Chen, J. Biesiadecki, *Space Sci. Rev.* **2020**, *217*, 5.
[4] G. R. Osinski, M. Battler, C. M. Caudill, R. Francis, T. Haltigin, V. J. Hipkin, M. Kerrigan, E. A. Pilles, A. Pontefract, L. L. Tornabene, P. Allard, J. N. Bakambu, K. Balachandran, D. W. Beaty, D. Bednar, A. Bina, M. Bourassa, F. Cao, P. Christoffersen, B.-H. Choe, E. Cloutis, K. Cote, M. Cross, B. D'Aoust, O. Draz, B. Dudley, S. Duff, T. Dzamba, P. Fulford, E. Godin, J. Goordial, A. Grau Galofre, T. Haid, E. Harrington, T. Harrison, J. Hawkswell, D. Hickson, P. Hill, L. Innis, D. King, J. Kissi, J. Laughton, Y. Li, E. Lymer, C. Maggiori, M. Maloney, C. L. Marion, J. Maris, S. Mcfadden, S. M. McLennan, A. Mittelholz, Z. Morse, J. Newman, J. O'Callaghan, A. Pascual, P. Patel, M. Picard, I. Pritchard, J. T. Poitras, C. Ryan, H. Sapers, E. A. Silber, S. Simpson, R. Sopoco, M. Svensson, G. Tolometti, D. Uribe, R. Wilks, K. H.

Williford, T. Xie, W. Zylberman, *Planet. Space Sci.* **2019**, *166*, 110.

[5] C. M. Caudill, A. J. Pontefract, G. R. Osinski, L. L. Tornabene, E. A. Pilles, M. Battler, R. Francis, E. Godin, A. Grau Galofre, T. Haltigin, V. J. Hipkin, A. Mittelholz, J. Poitras, S. L. Simpson, M. Svensson, T. Xie, Z. R. Morse, *Planet. Space Sci.* **2019**, *172*, 43.

[6] C. M. Caudill, G. R. Osinski, E. Pilles, H. M. Sapers, A. J. Pontefract, R. Francis, S. Duff, J. Laughton, J. O'Callaghan, R. Sopoco, G. Tolometti, M. Tuite, K. H. Williford, T. Xie, *Planet. Space Sci.* **2019**, *176*, 104682.

[7] Z. R. Morse, E. Harrington, P. J. A. Hill, P. Christoffersen, J. Newman, B.-H. Choe, L. L. Tornabene, C. Caudill, G. R. Osinski, *Planet. Space Sci.* **2019**, *168*, 15.

[8] M. A. Sephton, R. W. Court, J. M. Lewis, M. C. Wright, P. R. Gordon, *Planet. Space Sci.* **2013**, *78*, 45.

[9] L. L. Tornabene, M. Battler, B.-H. Choe, G. R. Osinski, *Planet. Space Sci.* **2019**, *173*, 14.

[10] J. M. Stromberg, A. Parkinson, M. Morison, E. Cloutis, N. Casson, D. Applin, J. Poitras, A. M. Marti, C. Maggiori, C. Cousins, L. Whyte, R. Kruzelecky, D. Das, R. Leveille, K. Berlo, S. K. Sharma, T. Acosta-Maeda, M. Daly, E. Lalla, *Planet. Space Sci.* **2019**, *176*, 104683.

[11] P. C. Joshi, K. Dubey, M. F. Aldersley, M. Sausville, *Biochem. Biophys. Res. Commun.* **2015**, *462*, 99.

[12] J. M. Kotler, N. W. Hinman, C. D. Richardson, A. G. Conly, J. R. Scott, *Planet. Space Sci.* **2009**, *57*, 1381.

[13] T. Haltigin, C. Lange, R. Mugnuolo, C. Smith, iMARS Working Group (2016), T. Haltigin, C. Lange, R. Mugnolo, C. Smith, H. Amundsen, P. Bousquet, C. Conley, A. Debus, J. Dias, P. Falkner, V. Gass, A.-M. Harri, E. Hauber, A. Ivanov, A. Ivanov, G. Kminek, O. Korablev, D. Koschny, J. Larranaga, B. Marty, S. McLennan, M. Meyer, E. Nilsen, P. Orleanski, R. Orosei, D. Rebuffat, F. Safa, N. Schmitz, S. Siljeström, N. Thomas, J. Vago, A.-C. Vandaele, T. Voirin, C. Whetsel, *Astrobiology* **2018**, *18*, 131.

[14] C. García-Florentino, I. Torre-Fdez, P. Ruiz-Galende, J. Aramendia, K. Castro, G. Arana, M. Maguregui, S. F. Ortiz de Vallejuelo, J. M. Madariaga, *Talanta* **2020**, *224*, 121863.

[15] S. S. Russell, L. Folco, M. M. Grady, M. E. Zolensky, R. Jones, K. Righter, J. Zipfel, J. N. Grossman, *Meteorit. Planet. Sci.* **2004**, *39*, 215.

[16] P. Gillet, J. A. Barrat, P. Beck, B. Marty, R. C. Greenwood, I. A. Franchi, M. Bohn, J. Cotten, *Meteorit. Planet. Sci.* **2005**, *40*, 1175.

[17] E. L. Walton, A. J. Irving, T. E. Bunch, C. D. K. Herd, *Meteorit. Planet. Sci.* **2012**, *47*, 1449.

[18] T. Mikouchi, *Meteorit. Planet. Sci.* **2005**, *40*, 1621.

[19] T. Mikouchi, T. Kurihara, *Pol. Sci.* **2008**, *2*, 175.

[20] K. Nagao, J. Park, H. G. Choi, *Pol. Sci.* **2008**, *2*, 195.

[21] C. Meyer, *NASA report on NWA 1950. NWA 1950–797 grams. Intermediate Diabasic Shergottite (2 stones)*, NASA, Martian Meteorite Compedium, **2012**.

[22] E. L. Walton, C. D. K. Herd, *Meteorit. Planet. Sci.* **2007**, *42*, 63.

[23] B. van de Moortèle, B. Reynard, P. Rochette, M. Jackson, P. Beck, P. Gillet, P. F. McMillan, C. A. McCammon, *Earth Planet. Sci. Lett.* **2007**, *262*, 37.

[24] B. van de Moortèle, B. Reynard, P. F. McMillan, M. Wilson, P. Beck, P. Gillet, S. Jahn, *Earth Planet. Sci. Lett.* **2007**, *261*, 469.

[25] T. G. Sharp, P. S. de Carli, Shock Effects in Meteorites, in *Meteorites and the Early Solar System II*, the University Press, Tucson **2006** 653.

[26] K. Castro, M. Pérez-Alonso, M. D. Rodríguez-Laso, L. A. Fernández, J. M. Madariaga, *Anal. Bioanal. Chem.* **2005**, *382*, 248.

[27] R.T. Downs. The RRUFF Project: An Integrated Study of the Chemistry, Crystallography, Raman and Infrared Spectroscopy of Minerals, *Program and Abstracts of the 19th General Meeting of the International Mineralogical Association in Kobe, Japan*, **2006**.

[28] L. B. Breitenfeld, M. D. Dyar, C. J. Carey, T. J. Tague Jr., P. Wang, T. Mullen, M. Parente, *Am. Mineral.* **2018**, *103*, 1827.

[29] K. E. Kuebler, B. L. Jolliff, A. Wang, L. A. Haskin, *Geochim. Cosmochim. Acta* **2006**, *70*, 6201.

[30] I. Torre-Fdez, C. Garcia-Florentino, J. Huidobro, L. Coloma, P. Ruiz-Galende, J. Aramendia, K. Castro, G. Arana, J.M. Madariaga, Characterization of Olivines and their Metallic Composition: Raman Spectroscopy Could Provide an Accurate Solution for the Active and Future Mars Missions, EPSC2021–586, **2021**.

[31] D. L. A. de Faria, S. Venâncio Silva, M. T. de Oliveira, *J. Raman Spectrosc.* **1997**, *28*, 873.

[32] L. Wang, X. Lu, C. Han, R. Lu, S. Yang, X. Song, *CrstEngComm* **2014**, *16*, 10618.

[33] R. Michel, M. R. Ammar, J. Poirier, P. Simon, *Ceram. Int.* **2013**, *39*, 5287.

[34] O. Shebanova, P. Lazor, *J. Solid State Chem.* **2003**, *174*, 424.

[35] X.-F. Qu, Q.-Z. Yao, G.-T. Zhou, S.-Q. Fu, J.-L. Huang, *J. Phys. Chem. C* **2010**, *114*, 8734.

[36] S. A. T. Redfern, K. S. Knight, C. M. B. Henderson, B. J. Wood, *Mineral. Mag.* **1998**, *62*, 607.

[37] Q. Dong, X. Liu, W. Zhang, *Opt. Mater. Express, OME* **2019**, *9*, 3519.

[38] L. Bindi, S.-H. Shim, T. G. Shim, X. X. Sharp, *Sci. Adv.* **2020**, *6*, eaaay7893.

[39] E. Huang, C. H. Chen, T. Huang, E. H. Lin, J.-A. Xu, *Am. Mineral.* **2000**, *85*, 473.

[40] D. M. Buchs, R. A. Howie, *Reference Module in Earth Systems and Environmental Sciences*, Elsevier, Amsterdam, Netherlands **2016**.

[41] S. Shkolyar, S. J. Jaret, B. A. Cohen, J. R. Johnson, O. Beyssac, J. M. Madariaga, R. C. Wiens, A. Ollila, S. Holm-Alwmark, Y. Liu, *Earth, Moon & Plan.* **2022**, *126*, 4.

[42] S. K. Sharma, B. Simons, H. S. Yoder Jr., *Amer. Min.* **1983**, *68*, 1113.

[43] C. E. Vennari, Q. Williams, *Phys. Chem. Miner.* **2021**, *48*, 34.

[44] J. E. Rodrigues, M. M. Ferrer, T. R. Cunha, R. C. Costa, J. R. Sambrano, A. D. Rodrigues, P. S. Pizani, *J. Phys. Condens. Matter* **2018**, *30*, 485401.

[45] M. M. Ramakokovhu, P. A. Olubambi, R. K. K. Mbaya, T. Mojisola, M. L. Teffo, *Minerals* **2020**, *10*, 1022.

[46] V. D'Ippolito, G. B. Andreozzi, D. Bersani, P. P. Lottici, *J. Raman Spectrosc.* **2015**, *46*, 1255.

[47] D. Lenaz, V. Lughi, *Phys. Chem. Miner.* **2013**, *40*, 491.

[48] A. Wang, K. E. Kuebler, B. L. Jolliff, L. A. Haskin, *Am. Mineral.* **2004**, *89*, 665.

[49] M. Jia, K. Zhai, M. Gao, W. Wen, Y. Liu, X. Wu, S. Zhai, *Vib. Spectrosc.* **2020**, *106*, 103005.

[50] M. Y. Fong, M. Nicol, *J. Chem. Phys.* **1971**, *54*, 579.

[51] P. K. Narayanaswamy, *Proc. Indiana Acad. Sci.* **1947**, *26*, 511.

[52] T. Pippinger, R. Miletich, M. Merlini, P. Lotti, P. Schouwink, T. Yagi, W. A. Crichton, M. Hanfland, *Phys. Chem. Miner.* **2015**, *42*, 29.

[53] J. Podder, R. Kobayashi, M. Ichimura, *Thin Solid Films* **2005**, *472*, 71.

[54] O. Alekperov, Z. Jahangirli, R. Paucar, *Phys. Status Solidi B* **2016**, *253*, 2049.

[55] S. I. Sadovnikov, E. Y. Gerasimov, *Nanoscale Adv.* **2019**, *1*, 1581.

[56] F. Selsis, in *Encyclopedia of Astrobiology*, (Eds: M. Gargaud, R. Amils, J. C. Quintanilla, H. J. [. J.]. Cleaves, W. M. Irvine, D. L. Pinti, M. Viso), Springer, Berlin, Heidelberg **2011** 1195.

SUPPORTING INFORMATION

Additional supporting information can be found online in the Supporting Information section at the end of this article.